#### **PAPER**

## Microwave emissions from the cold atmospheric helium plasma jet

To cite this article: Yi Liu et al 2023 Plasma Sources Sci. Technol. 32 095012

View the article online for updates and enhancements.

#### You may also like

- ON THE DETECTABILITY OF DUAL JETS FROM BINARY BLACK HOLES Philipp Moesta, Daniela Alic, Luciano Rezzolla et al.
- <u>Harmonic Radio Emission in Randomly Inhomogeneous Plasma</u>
  Anna Tkachenko, Vladimir Krasnoselskikh and Andrii Voshchepynets
- Electromagnetic Emission from Blitzars and Its Impact on Non-repeating Fast Radio Bursts

Elias R. Most, Antonios Nathanail and Luciano Rezzolla



Plasma Sources Sci. Technol. 32 (2023) 095012 (14pp)

https://doi.org/10.1088/1361-6595/acf7e9

# Microwave emissions from the cold atmospheric helium plasma jet

Yi Liu<sup>1,2</sup>, Li Lin<sup>1</sup> and Michael Keidar<sup>1,\*</sup>

E-mail: keidar@gwu.edu

Received 10 July 2023, revised 2 September 2023 Accepted for publication 8 September 2023 Published 19 September 2023



#### **Abstract**

One of the recently observed effects of plasma in medical applications is the physical effect, suggesting that the electromagnetic (EM) emission of cold atmospheric plasmas can lead to cell membrane oscillations and sensitization to the chemical active ingredient of treatments such as cancer drugs. This is a new aspect that must be considered along with the plasma chemical effects for the future dose definition which is the most urgent research topic of plasma medicine. However, unlike the reactive oxygen and nitrogen species generated from plasma chemistry which is well-known as playing a key role in apoptosis cancer cells, the EM emission power spectrum and emission mechanism are still unquantified. This makes the uncertainty of the physical dosage of the therapy and thus impedes the further understanding and optimization of the plasma therapy. In this paper, we compute the 3D spatial distribution of the power density spectrum of EM emission from a cold atmospheric helium plasma jet. The simulations indicate that the plasma oscillations following the plasma streamer propagation are the main source of EM emission, while the emissions of the bulk current caused by net charge movements and the bremsstrahlung due to charge collisions are negligible. The results are also verified by a microwave power measurement using a heterodyne frequency sweep. These findings will thus fill out the last missing piece of the jigsaw before the plasma medicine community can define the dose in the future.

Keywords: low-temperature plasma, cold atmospheric plasma, plasma medicine, particle-in-cell, streamer, plasma oscillation

(Some figures may appear in colour only in the online journal)

#### 1. Introduction

Over the last decade, plasma medicine research focused on direct and indirect treatments in the field of plasma medicine [1, 2], especially plasma-based cancer therapy [3–5]. It has been reported repeatedly that short-lived species and physical effects such as radiofrequency (RF) emissions can strengthen the treatments in addition to the long-lived species such as the H<sub>2</sub>O<sub>2</sub> [6, 7]. However, a recent report indicates that the

physical effect can be a stand-alone treatment which can also lead to the death of cancer cells after some special cellular behaviors [8]. Such a physical effect may also have the potential for other plasma medicine applications where cells are interacting directly with the plasma plume [1, 2, 9, 10]. Moreover, the specific pathways are significantly different between the physical treatment and the conventional chemical ones, such as the selectivity of regular cold atmospheric plasma (CAP) treatment upon U87MG (human primary glioblastoma) and hTERT/E6/E7 (human astrocyte) [11]. The physical effects also include damage to the cellular membrane due to the physically induced osmotic pressure unbalance as

<sup>&</sup>lt;sup>1</sup> School of Engineering and Applied Science, The George Washington University, Washington, DC 20052, United States of America

<sup>&</sup>lt;sup>2</sup> School of Mechanical Engineering, Shanghai Jiao Tong University, Shanghai 200240, People's Republic of China

<sup>\*</sup> Author to whom any correspondence should be addressed.

a newly found type of necrosis that cannot be achieved by the conventional CAP chemical treatment [11]. The in-vitro physical treatment was achieved by treating the CAP jet on B16F10 (human melanoma cell line) colonies with a cover to block both chemical species and UV from the plasma [8]. In other words, the physical effect is a result of electromagnetic (EM) emissions lower than THz. Therefore, two highly suspicious frequency ranges should be considered which might be responsible for this physical effect. The first one is around 10– 15 GHz as a result of the plasma oscillation considering the regular plasma jet used for cancer treatment is at around 10<sup>10</sup>–  $10^{14}$  cm<sup>-3</sup> [12–15]. The second one is at the plasma jet's discharge frequency, which is the repetition of the impact of the high-voltage streamer head at kHz frequency [16]. The cells' response to the kHz effects was recently observed by Lin et al using a laser Michelson interferometer [17]. The cell membrane oscillates under such an emission due to the membrane potential, and the in-situ damage leads to blebbing and finally both apoptosis and necrosis [17] which agrees with other previous observations [8, 11].

The physical effects are thus an equally important aspect along with the chemical effects. Currently, the most urgent task of the plasma medicine community is to define the dose of the plasma treatment, and some work has been done based on the chemical pathways and reactive oxygen and nitrogen species (RONS) quantifications [18, 19]. However, since the physical effects are now confirmed, the dose must be redefined after the physical emissions of CAP are well investigated. Unfortunately, detailed measuring of the power spectrum of the plasma RF emission is still not quantified and it is not an easy task, although there was some related early works such as the measurement of the magnetic field of the plasma jet [20]. Due to the antenna size of collecting the emission, which is several centimeters, one will lose the spatial resolution in the vicinity of the plasma jet which is also a centimeterlarge area. Also, because of the pulse-like streamer generation with a repetition rate at kHz and pulse width at microseconds, it is impossible to have such a high temporal resolution for most of the RF power meters on the market. Therefore, in this work, a 3D mathematical model is developed to compute the power density distribution field of the plasma jet. Once the computation for each time step is completed, the results will be both spatially and temporally resolved. Therefore, these results provide more detailed information than the previously reported measurements since the temporal resolution of the latter is not possibly high enough to show the dynamic emission variation during a micro-second scale plasma bullet propagation. This work thus reveals the exact RF fields at the microwave band that the cells are exposed to, and it will be an important basis for the future discovery of the mechanism behind the physical effects of plasma cancer treatments.

#### 2. Simulation setups

The numerical simulation is achieved in MATLAB using the PIC algorithm. The simulation setup includes two parts. First, a 2D helium-guided plasma jet is simulated to provide streamer propagation which includes detailed plasma chemistry in the open air. The results include temporal and spatial resolved electron distribution, electron, and ion currents, etc. Next, the 2D simulation results will be rotated surrounding the central axis to become a 3D cylinder emission source with each grid in the meshed simulation domain thus considered as a small antenna. The antenna currents can thus be acquired by using the 2D simulation results. Three types of potential emission sources are included in this work: the plasma oscillation, the bulk current as the net charge movements, and the bremsstrahlung due to charge collisions. These three currents are within the GHz RF range to be compared and discussed.

#### 2.1. The 2D plasma jet simulation setups

A cold atmospheric helium plasma jet (CAPJ) as the emission source of the EM field must first be simulated to obtain the electric field distribution, electron density, electron velocity, etc. The simulation domain with the CAPJ nozzle is illustrated in figure 1(a), and it is meshed into 0.5 mm by 0.5 mm square grids making the grid number 12 000 in total. Two electrodes with constant potential boundary conditions are shown in the figure. The anode is selected from 6000 V and 8000 V which are two cases to compare the results, while the cathode is set up to the ground.

The 2D simulation of CAPJ starts with the assumption of initial seed electron distribution and the helium-air distribution in the 2D simulation domain. The distribution is based on an actual helium flow rate and the nozzle diameter of the CAPJ generator that was published previously [21]. Therefore, without a time-consuming massive discharge period of the simulation, assuming the initial species distribution as the steady state of the plasma jet, especially the seed electron distribution, is inevitable. The initial species distribution is shown in figure 2. The nozzle and the plasma propagation track are filled with helium, He<sup>+</sup>, and seed electrons, while their densities are decreasing far away from the high-voltage electrode. The ratio of the  $N_2$ ,  $O_2$ , and  $H_2O$  in the air is 0.797:0.198:0.005 outside the nozzle. All other minor-important species share the same distribution similar to the N2 but with a low amplitude.

The simulation flow chart is shown in figure 3. First, a 2D Poisson solver is applied to obtain the electric field based on the information on boundary conditions and the initial charges. This is followed by a PIC algorithm that is then used to solve electrodynamics in the whole calculation domain to move the electrons. Next, in each grid, a kinetic scheme of plasma chemistry containing more than 40 species with 448 chemical reactions is considered for plasma chemistry [13, 22–24]. The kinetic scheme database is listed in the supplementary materials. The chemical reaction rates are determined by reactant concentrations and the rate coefficients that are theoretical functions of reactant temperatures. The electron temperature can be obtained by the Boltzmann equation solver BOLSIG+ with the LXCat collision cross-section database that is also used

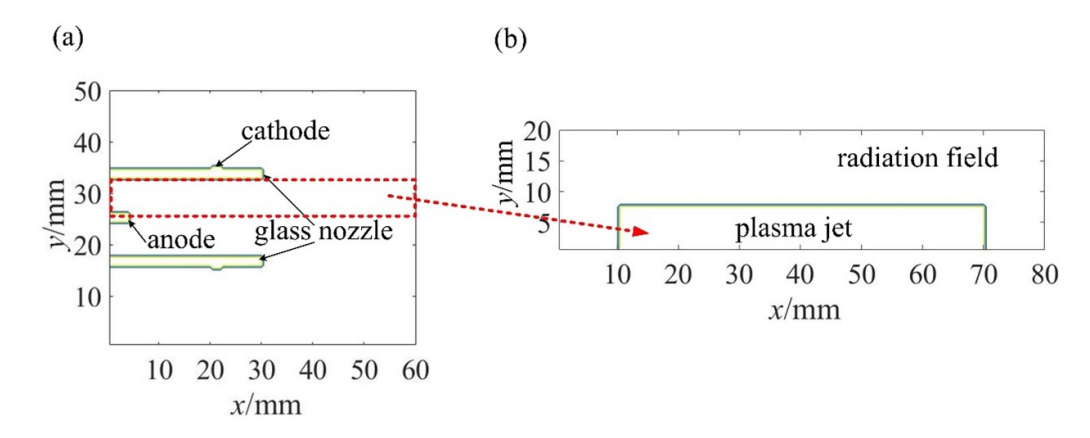


**Figure 1.** The geometry setup of the 2D simulation of the plasma jet. (a) The simulation domain of the plasma jet simulation. (b) The simulation domain of the RF emissions.

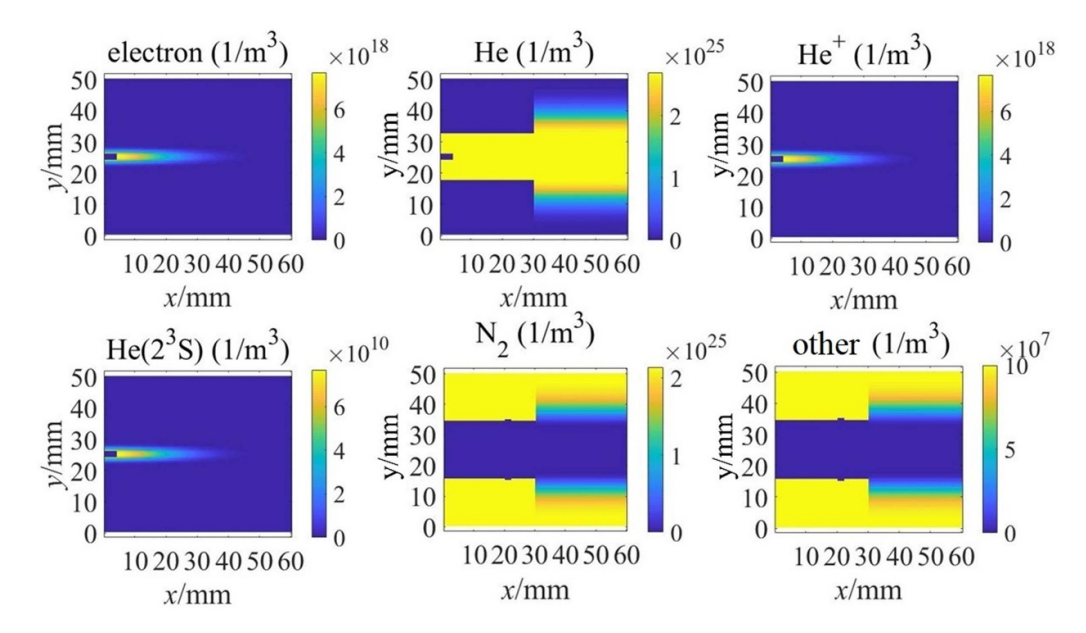


Figure 2. Initial species distributions of the plasma jet simulation. The  $O_2$  distribution is the same as the  $N_2$  but at a different amplitude. The subtitle 'other' represents the distribution of all other minor species.

for the chemical reaction computation in each grid [25, 26]. Therefore, the species distributions in the calculation domain can be updated in each iteration after both solving the electron movement driven by the electric field and solving the chemical reactions affected by the previous species distributions and the electron temperature.

#### 2.2. The computation method of 3D RF emissions

To compute the 3D RF emission, one needs to define the radiation source as shown in figure 1(b). The source area consists of two parts that are plasma jet region and the radiation field region. The entire calculation domain meshes into  $0.5 \text{ mm} \times 0.5 \text{ mm}$  rectangular grids, which means 6400 grids in total. In such a source area, each grid is considered as a small linear wire antenna that will emit RF in 3D as shown in figure 4(a). Next, the 2D source area will rotate to provide a 3D source area as shown in figure 4(b).

Each cell in the calculation domain of the emission source is assumed as a small linear wire antenna unit contributing to the total emission. Therefore, the total radiation can be calculated as the superposition of emissions from all antennas. Note that in this approach we assume plasma to be optically thin and as such, we neglect absorption by the plasma. Figure 4(a) presents the electric-field orientation of a linear wire antenna, in which  $\varphi$ ,  $\theta$ , and r indicate the location relationship between the antenna source S and the receiver T. The components of electric field E can thus be computed as [27]

$$E_{\varphi} = 0 \tag{1}$$

$$E_r = \eta \frac{I_0 l \cos \theta}{2\pi r^2} \left[ 1 + \frac{1}{jkr} \right] e^{-jkr} \tag{2}$$

$$E_{\theta} = j\eta \frac{kI_0 l \sin \theta}{4\pi r} \left[ 1 + \frac{1}{jkr} - \frac{1}{(kr)^2} \right] e^{-jkr}.$$
 (3)

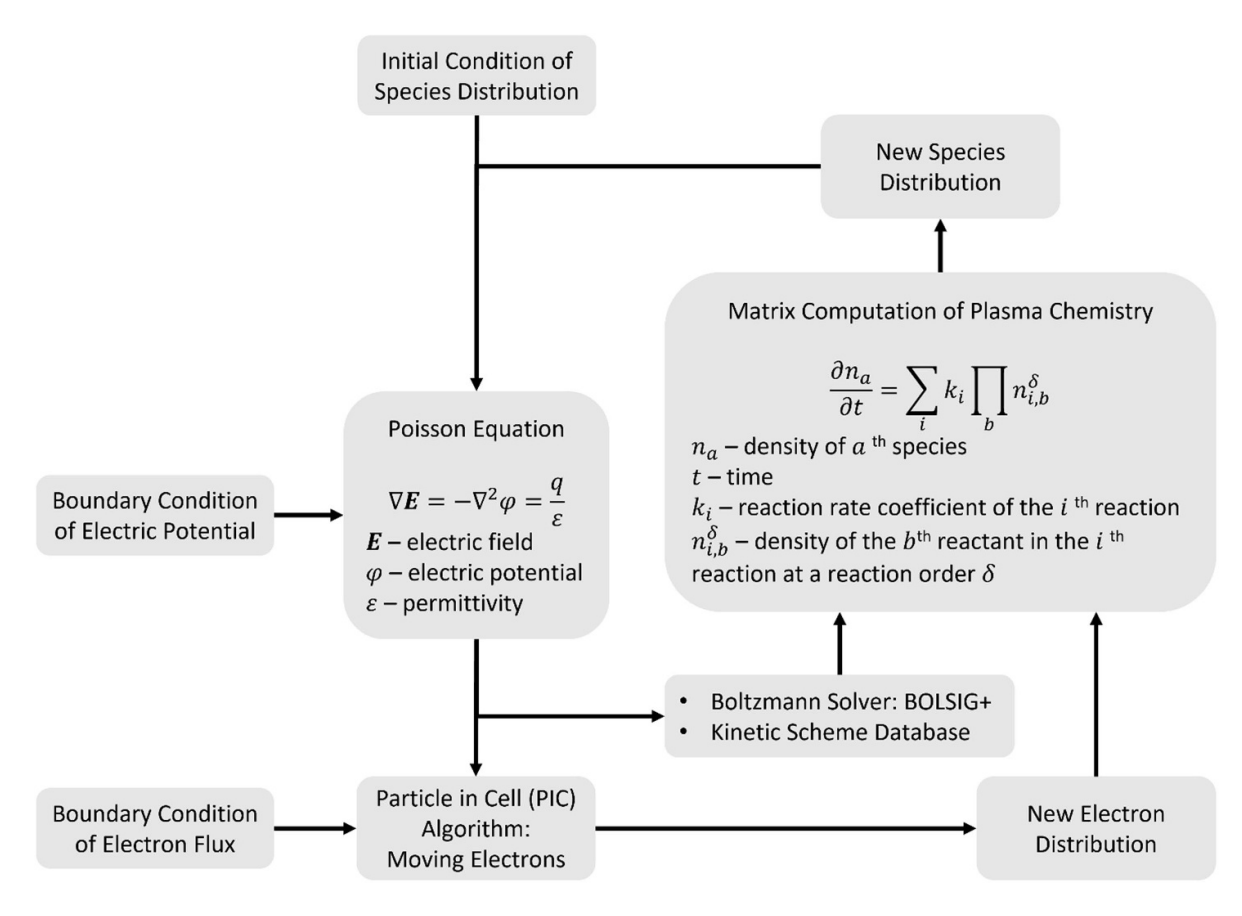
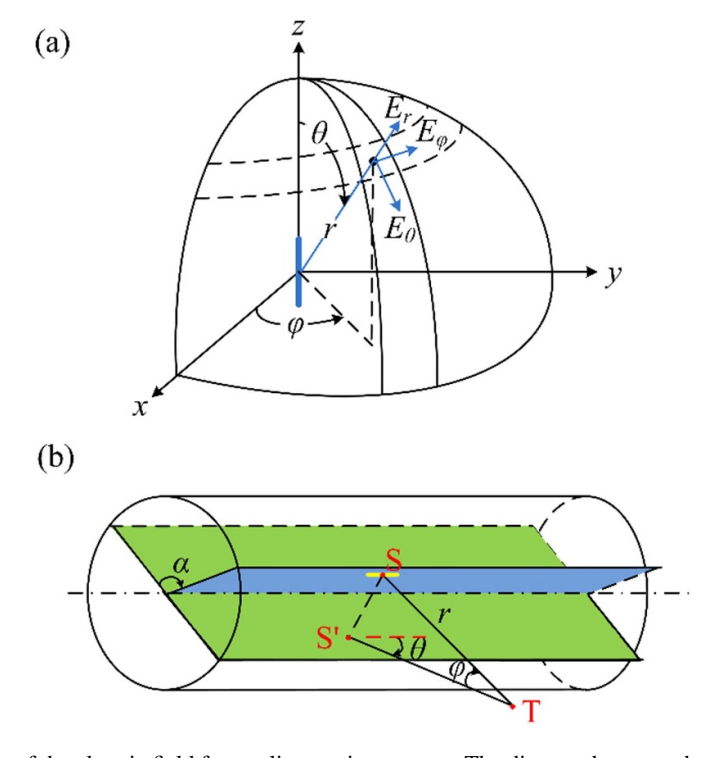


Figure 3. The flowchart of the 2D simulation of the plasma jet.



**Figure 4.** (a) Schematic diagram of the electric field from a linear wire antenna. The distance between the source antenna and the receiver is r. The azimuthal angle and the zenith angle are denoted as  $\varphi$  and  $\theta$  respectively. The components of electric field E are thus defined in the figure. (b) The geometrical relationship between the emission sources S and the receiver T, while the 2D source plane is at angle  $\alpha$  from the horizontal plane containing the point S' as the projection of S.

In these equations,  $\eta$  is the vacuum impedance,  $I_0$  is the current, l is the antenna length, k is the wavenumber, and j is the imaginary unit. Meanwhile, the components of the magnetic field H are described as [27]

$$H_r = H_\theta = 0 \tag{4}$$

$$H_{\varphi} = j \frac{kI_0 l \sin \theta}{4\pi r} \left[ 1 + \frac{1}{jkr} \right] e^{-jkr}. \tag{5}$$

The Poynting vector is formed in terms of the electric field and the magnetic field radiated by the antenna. The components of the Poynting vector  $\mathbf{W}$  are given, respectively, as [27]

$$W_{\varphi} = 0 \tag{6}$$

$$W_r = \frac{\eta}{8} \left| \frac{I_0 l}{\lambda} \right|^2 \frac{\sin^2 \theta}{r^2} \left[ 1 - j \frac{1}{(kr)^3} \right]$$
 (7)

$$W_{\theta} = j\eta \frac{k|I_0 l|^2 \sin \theta \cos \theta}{16\pi^2 r^3} \left[ 1 + \frac{1}{(kr)^2} \right]$$
 (8)

in which  $\lambda$  is the wavelength.

The plasma emission source needs to be considered as a 3D space because the emission power from a pair of symmetrical source points cannot be canceled out, thus every cell in this 3D space contributes to the emission power of receivers. However, a 2D radiation field can be used due to azimuthal symmetry. Figure 4(b) displays the geometrical relationship between the emission source and the receiver. Point S' is the projection of point S on the green plane which is the plane where the receiver T is located. The Poynting vector at receiver point T from the emission source S thus can be calculated by equations (6)–(8). The total emission received at point T is the superposition of the Poynting vectors from all the emission source points in the plasma region. Then, we can obtain the radiation field by calculating the emissions at every receiver point.

The plasma source theoretically has three types of emissions that are bulk current emission, plasma oscillation emission, and bremsstrahlung emission [28, 29]. We calculated these three types of emissions respectively since they have different generation mechanisms. As the plasma streamer propagates, the net charge movements in the plasma produce the bulk current emission. Each bulk current in the calculation grid is assumed as a small linear wire antenna. The antenna length (l), current  $(I_0)$ , and wavenumber (k) are given, respectively, by

$$l = v_e dt \tag{9}$$

$$I_0 = e n_e v_e h^2 \tag{10}$$

$$k = \frac{f}{c}. (11)$$

In the equations, e is the electron charge,  $n_e$  is the electron density,  $v_e$  is the electron velocity, h is the grid size, t is time, c is the speed of light, and the discharge frequency f is 12.5 kHz [13, 21, 30], with the dt set at 0.1 ns in the computation. Therefore, the radiation field of the bulk current emission can be calculated by equations (6)–(11).

The positive ions attract electrons causing plasma oscillations. The effective electron velocity of the oscillation ( $V_{\rm eff}$ ) is calculated by equation [31]

$$V_{\text{eff}} = V_0 - \frac{ek\varphi_0}{m_e} \frac{\exp\left[j(kx_0 - \omega t_0)\right]}{\omega - kV_0} \exp$$

$$\times \left[j(kV_0 - \omega)(t - t_0) - 1\right] \tag{12}$$

where  $x_0$ ,  $V_0$ ,  $\varphi_0$  refer to the position, velocity, and electric potential when the electron cloud enters the ions at the time  $t_0$ , and  $m_e$  and  $\omega$  are the electron mass and the oscillation frequency, respectively. Each electron cloud movement caused by the plasma oscillation is assumed as a tiny antenna. Different from the equations of the bulk current emission, the antenna length, current, and wave number in the case of the plasma oscillation is given as

$$l = \frac{1}{2} \frac{2\pi V_{\text{eff}}}{\omega} \tag{13}$$

$$I_0 = e n_e V_{\text{eff}} h^2 \tag{14}$$

$$k = \frac{\omega}{2\pi V_{\text{eff}}}.$$
 (15)

Therefore, we can take these variables into equations (6)–(8) to calculate the radiation field from plasma oscillations.

Bremsstrahlung is the EM radiation produced by the deceleration of electrons during collisions. The mathematical expression of its power density  $P_{Br}$  produced by the bremsstrahlung emission and the frequency  $\omega_{Br}$  is given by [32]

$$\frac{\mathrm{d}P_{Br}}{\mathrm{d}\omega_{Br}} = A\left(1 - \frac{\omega_p^2}{\omega_{Br}^2}\right)^{\frac{1}{2}} (2\ln\omega_{Br} + B) \tag{18}$$

$$A = \frac{-8\sqrt{2}}{3\sqrt{\pi}} \left(\frac{e^2}{4\pi\,\varepsilon_0}\right)^3 \frac{1}{(m_e c^2)^{\frac{3}{2}}} \frac{Z_i^2 n_i n_e}{(k_B T_e)^{\frac{1}{2}}} \tag{19}$$

$$B = \ln\left(\frac{\hbar^2}{2k_B^2 T_e^2}\right) + C_0. \tag{20}$$

In these equations,  $\varepsilon_0$  is the vacuum permittivity,  $k_B$  is the Boltzmann constant,  $T_e$  is electron temperature,  $\hbar$  is the reduced Planck constant, and  $C_0$  is the Euler–Mascheroni constant. Assuming only electrons are moving in the plasma column because the electron mass is exceedingly small compared with other species, and the charge number  $Z_i$  and the ion density  $n_i$  in the equations thus equal to 1 and  $n_e$ , respectively.

However, there is another issue we need to concern that the plasma jet itself may absorb microwave radiation. More specifically, we need to consider if the emission from the center axis of the plasma jet can be partially absorbed by the plasma at the boundary of the jet. It is well known that plasma can block the incoming EM wave when the incoming frequency is lower than the plasma frequency which is proportional to the electron density as mentioned in equation (22). Therefore, the outer plasma can block the inner plasma only when the outer electron density is higher than the inner electron density. According to figure 7(c), the electron density at the center axis is always higher, therefore, no outer plasma can absorb the inner emissions. However, for some specific plasma jet hardware setups, the streamer can form in a donutlike pattern during a part of its propagation process, depending on the helium-air distribution, in other words, the helium flow rate and nozzle geometry [33]. In this case, a part of the low-frequency power from the center axis near the anode will be blocked, but the since the frequency spectrum is continuous (electron density distribution is continuous), the lowfrequency power can still be emitted from the plasma jet tip part where the donut-like pattern has merged into a dot-like bullet and the electron density is also low. In other words, the low-frequency part of the power spectrum can be blocked partially, rather than completely, when the streamer has a donut-like appearance. However, this situation cannot significantly change the general shape of the spectrum pattern, since the low-frequency part of the spectrum always has a lower power even without the blocking as shown in the previous figures.

#### 3. Experimental setups

As mentioned previously, the plasma oscillation is expected to be in the range of 10-15 GHz according to the electron density. The emission from the plasma jet is a frequency mixture with an unknown power spectrum to be measured. A WR-75 horn antenna aiming at 10–15 GHz (X to Ku band) is set to collect the emission. The signal will pass through a power amplifier (Mini-Circuits ZX60-138-S+) and finally reach the RF port of a frequency mixer (Fairview Microwave FMMX1029). On the other hand, a microwave generator (HP8350B Sweep Oscillator with HP86251A RF Plug-In) will provide a singlefrequency window to the local oscillator (LO) port of the frequency mixer, through a signal splitter (Mini-Circuits ZX10-2-183-S+). The splitter is mainly used to calibrate but will also be connected during the measurement to avoid changing the system. The microwave generator will sweep the frequency from 12–16 GHz. Therefore, for each frequency window provided by the microwave generator, the intermediate frequency (IF) port of the mixer will output the power within the window and the value will be measured by the microwave power meter (HP438A). The plasma jet is working at the 6000 V sinusoidal discharge voltage at 12.5 kHz with a 10 LPM helium flow rate. The schematic of the experimental measurement is shown in figure 5(a). However, as mentioned

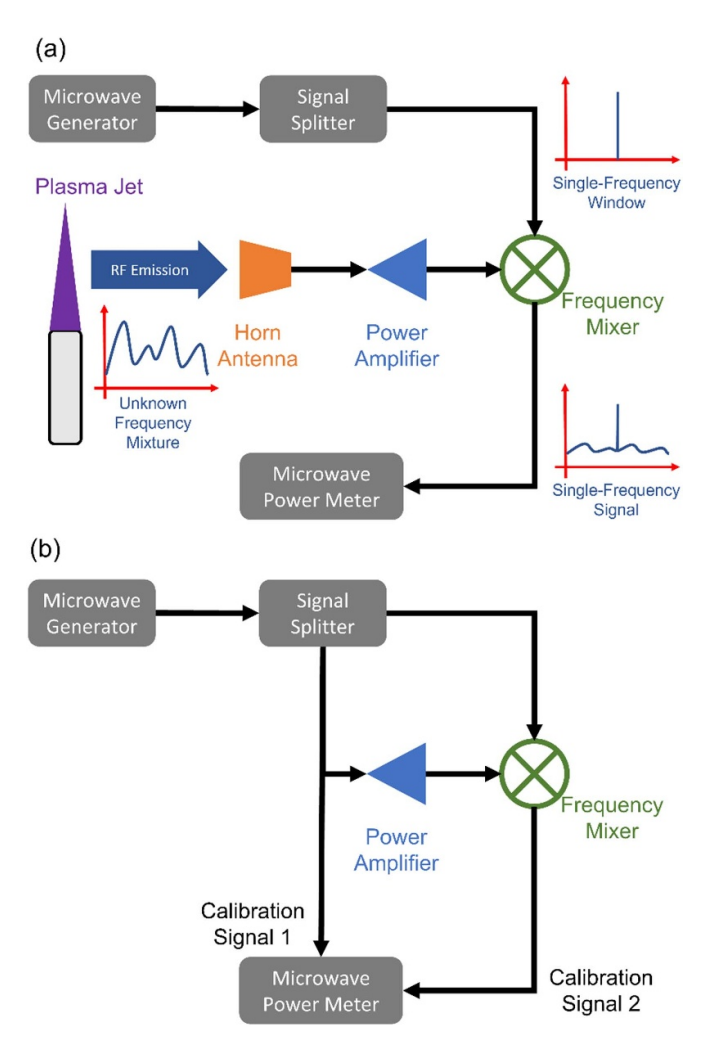


**Figure 5.** The schematic of the heterodyne setup to measure the power spectrum of the plasma jet. (a) The measurement setup. (b) The calibration setup.

at the end of the introduction, there is no spatial and temporal resolution of this measurement. The resulting power spectrum will be the spatially averaged power density at a distance of 1.5 cm from the plasma jet central axis. Also, because the signal is emitted from the streamer propagation pulse only, but the microwave power meter collects the entire discharge period, when acquiring the results, a scaling factor  $\frac{\tau_d}{\tau_s}$  will be applied, where  $\tau_d$  is the discharge period,  $\tau_s$  is the period of streamer propagation.

Also, as shown in figure 5(b), the system must be calibrated before making a measurement, due to the unknown signal losses in the coaxial cable connectors and the RF chips. Two calibration signals will be collected as shown in figure 5(b) with a frequency sweep from 12 GHz to 16 GHz by the microwave generator. A signal splitter will be used to separate the signal, one for the LO, and the other one is a mimic of the incoming RF signal as the calibration signal 1 to be recorded. The IF output denoted as calibration signal 2 will be divided by signal 1 to show the total net power loss of the system. The calibration result is shown in figure 6.

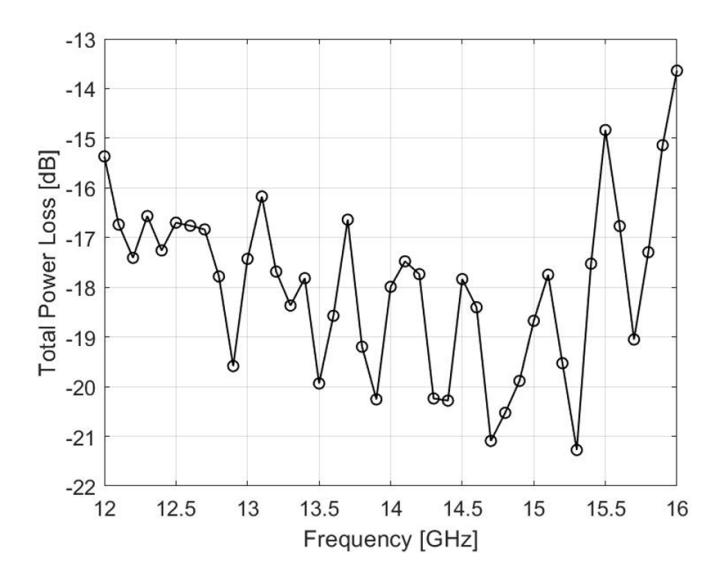


Figure 6. The calibration result of the heterodyne system.

Therefore, the final measurement result will be presented as

$$P(f) = S(f) \frac{\tau_d}{\tau_s} 10^{\frac{\text{Loss}}{10 \text{ dB}}}$$
 (21)

where P(f) is the final power spectrum result, f is the frequency axis, S(f) is the signal spectrum acquired from the microwave power meter, and Loss is the total power loss acquired in the calibration,  $\frac{\tau_d}{\tau_s}$  is the scaling factor as introduced above.

#### 4. Results and discussions

#### 4.1. The simulation results

The results including the evolutions of the electric field, ionization rate, and electron density are displayed in figure 7. At the initial stage, the highest electric field strength and the largest ionization rate are near the high-voltage electrode. Driven by the electric field, the streamer head which is the ionization wavefront (also known as 'plasma bullet') propagates away from the high-voltage anode, meanwhile, the renewed charge distribution changes the electric field. Please note that the electric field at the ionization wavefront looks insignificant in figure 7(a), although it looks higher than the surrounding. This is because the electric field near the electrodes is much stronger than the one at the ionization wavefront. The color bar scale is covering the entire electric field range and thus makes the ionization front electric field look faint. But the electric field at the wavefront is effectively leading to the local high ionization rate, which is the plasma bullet. The plasma bullet passes through the low-voltage cathode and finally exits the nozzle with a 45 mm maximum movement distance. The stronger electric field area gradually moves near the low-voltage electrode which also has a larger ionization rate. During the streamer propagation, the electron density shows a plasma track behind the anode, which has no obvious change over time. Also, please note that the streamer propagation does not necessarily have an electron density peak at the ionization wavefront. The electron density is highest near the anode, then gradually decreases along the plasma jet. There are many other simulation works showing the same results [34–37].

### 4.2. The results of 3D RF emission computation and microwave measurements

As previously mentioned, three types of radiation from the cold helium plasma jet are calculated including bulk current emission, plasma oscillation emission, and bremsstrahlung emission. First, the power densities from the bulk current emission and the plasma oscillation emission are displayed in figure 8(a). Here we mainly consider the power emission in the period when the streamer is propagating. Because after the streamer disappeared, the electron density decrease significantly as reported by many other publications, [38–40] and the emission power of the bulk current and plasma oscillation are proportional to the electron density. The power density decreases as the distance from the plasma jet increases. The maximum power density of the bulk current emission is on the order of  $10^{-17}$ – $10^{-22}$  W cm<sup>-2</sup> at couple centimeters away. The power density of plasma oscillation emission is shown in figure 8(b), and it is in the range of  $420-600 \text{ W cm}^{-2}$ . Integrating the plasma oscillation emission's power density over the plasma region, the total power is estimated at about 2.86 W emitted from the plasma. Considering the discharge voltage is at 8 kV and the discharge current is usually at about 10 mA in our device [39], there are about 3.5% of the discharge power transferred to the plasma oscillation. The power density emitted from the bulk current is very weak compared with the one from the plasma oscillation. Such a significant difference is not surprising in a highly collisional plasma, because the bulk current is computed based on the electron drift current while the plasma oscillation is based on the electron density. In a previous experimental measurement, the bulk current of a streamer propagation was found at about 0.8 mA with a discharge voltage at about 3.8 kV [39]. In this work, we have the bulk current at about 1.5 mA with a discharge voltage at 8 kV. A higher discharge voltage results in a higher plasma jet current. Therefore, we are not surprised that a mA current emission is weak.

Figure 8 also shows the spatially resolved radiation fields of the bulk current emission and the plasma oscillation emission, respectively. A relatively high-power-density area in the radiation field of the bulk current emission appears near the high-voltage electrode at initial and then moves in the x direction (the direction of plasma bullet movement) over time. This characteristic is the same as that of the electric field distribution as shown in figure 7(a). However, the high-power-density area in the radiation field of the plasma oscillation emission is always located near the high-voltage electrode without a movement, which is the same as the distribution of the electron density as shown in figure 7(c). Also, the electron velocity is proportional to the electric field strength. Therefore, it implies

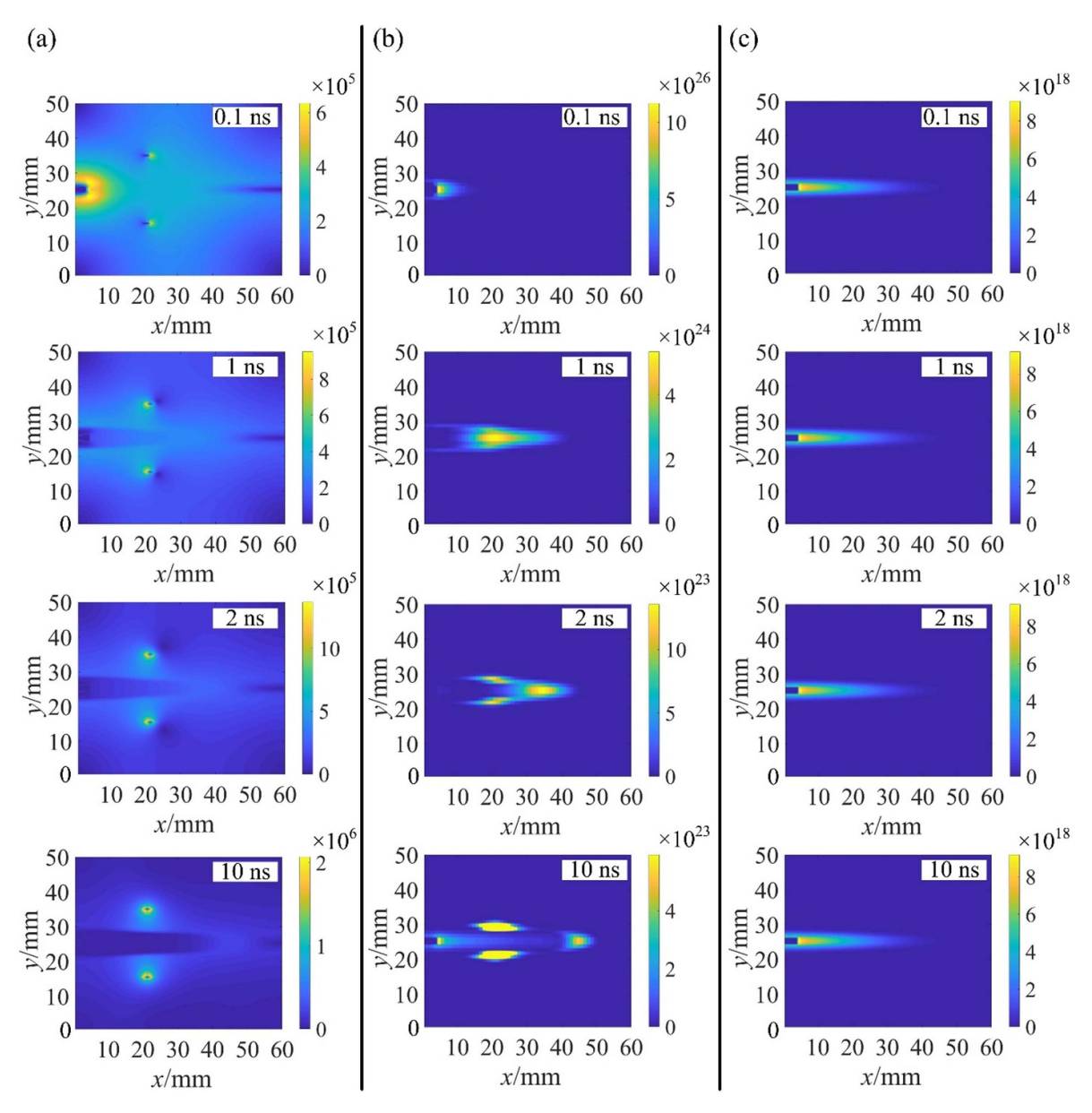


**Figure 7.** Simulation results of a cold atmospheric helium plasma jet: (a) electric field  $(V m^{-1})$ , (b) ionization rate  $(m^3 s^{-1})$ , and (c) electron density  $(1 m^{-3})$ .

that the electron velocity is the main effect factor of the power density produced by the bulk current, but the main effect factor of the plasma oscillation emission is the electron density of the plasma jet.

The advantage of studying this topic in a numerical simulation compared with the experimental measurement is to acquire spatial and temporal resolution. The spatial resolution includes the resolution of the emitting location and the receiver location. In other words, only through the numerical simulation, we can track the power density spectrum from a specific emission location in the plasma jet to a specific receiver location. The latter is important and practical while using the plasma treatment on a target such as a specific well in a 96-well plate or a specific location on the tissue such as melanoma (skin cancer).

First, in figure 9(a), an example background the to illustrate which region of the plasma jet is contributed to which line in the spectrum. Because the plasma frequency is proportional to the electron density that

$$\omega_p = \sqrt{\frac{n_e e^2}{m_e \varepsilon_0}} \tag{22}$$

the emitter frequency distribution shown in figure 9(a) is thus straightforward: the region closer to the anode should emit a higher frequency, which agrees with the electron density distribution shown in figure 7(c). Next, to find the specific spectra for the receiver at a different location, 3 locations marked as A, B, and C in the radiation field are chosen to show the

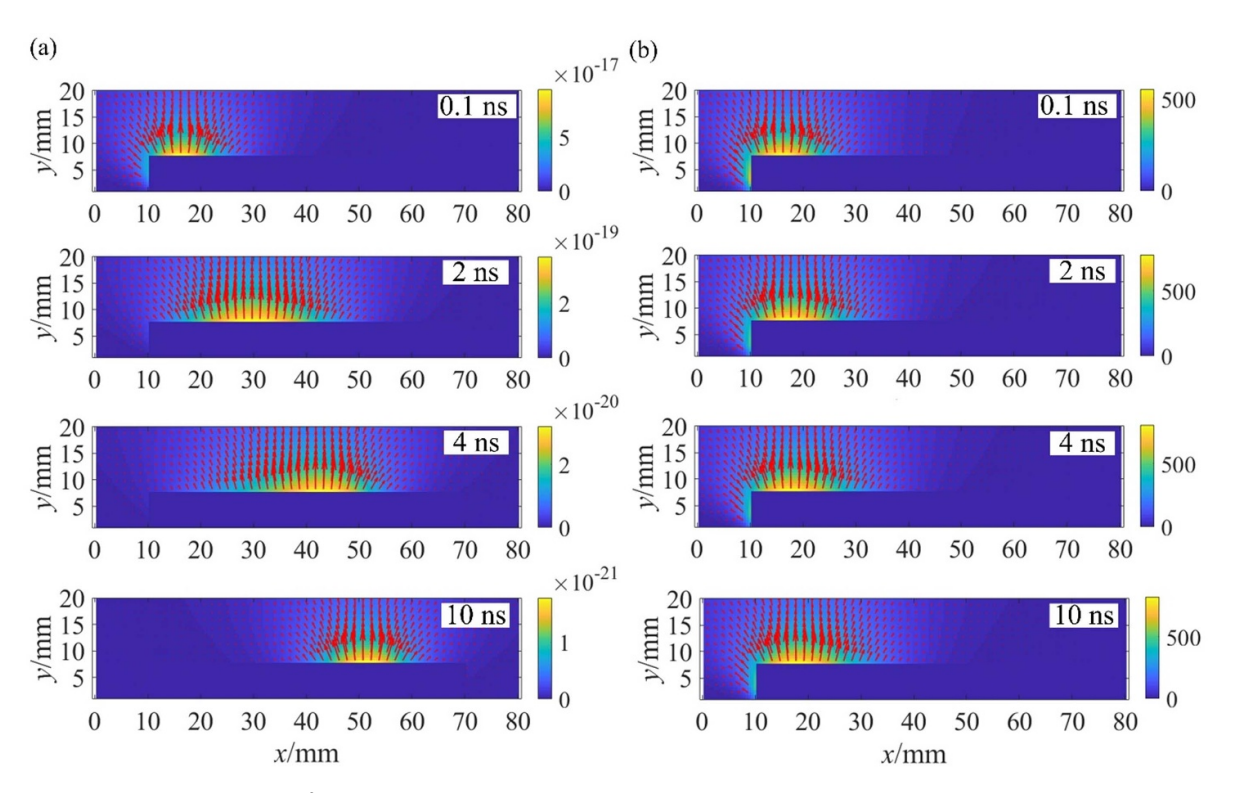
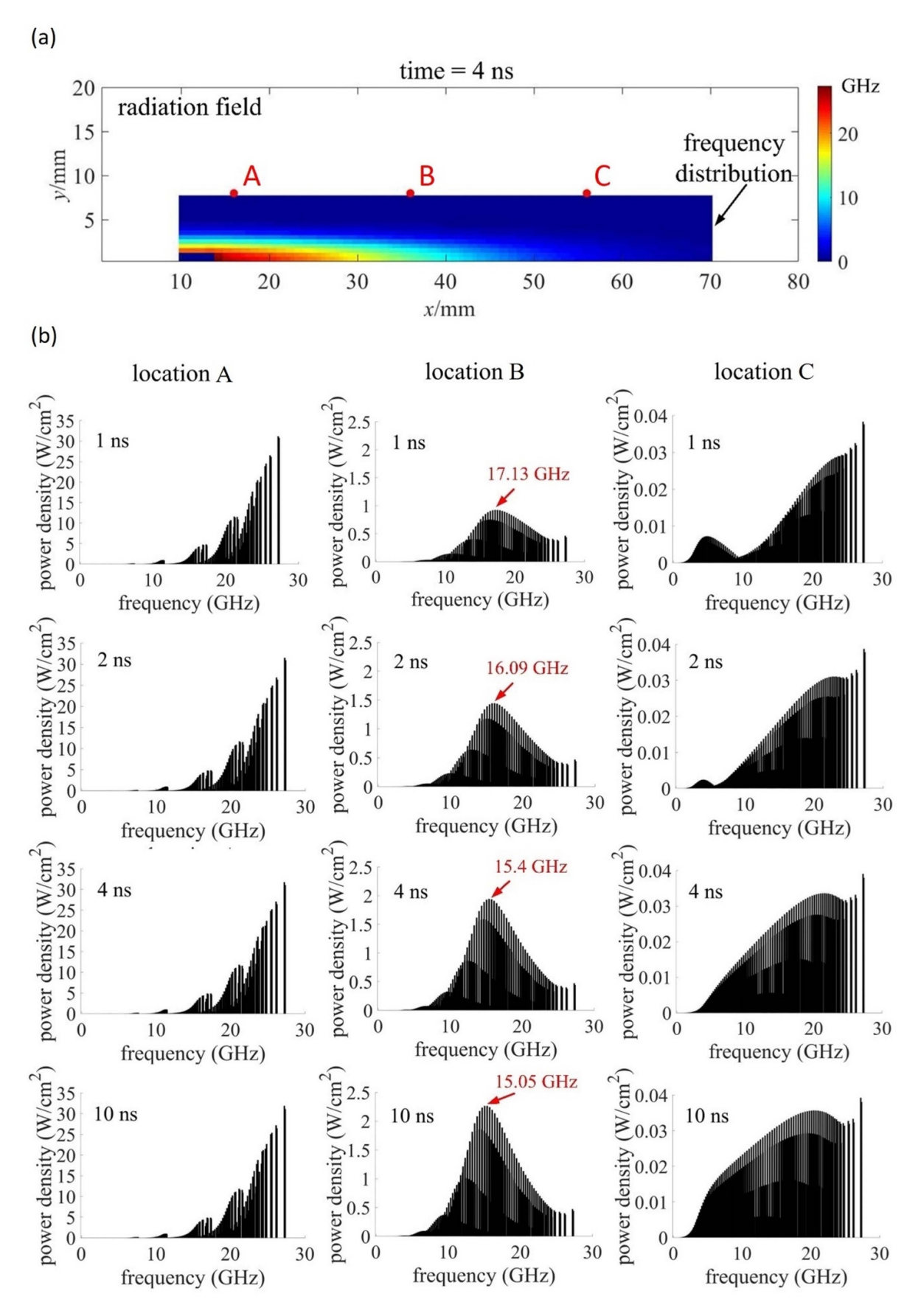


Figure 8. Power densities in  $(W \text{ cm}^{-2})$  of the two types of emissions from the plasma jet. (a) The bulk current emission. (b) The plasma oscillation emission. Note that the power densities are the total value as the integrations over the spectra which will be discussed later.

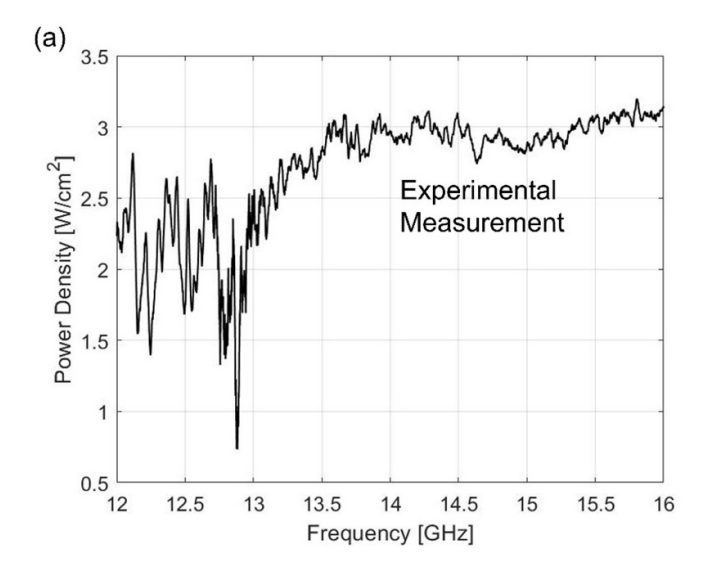
detailed spectra in figure 9(b) in 3 columns while the temporal evolution of these spectra is shown in rows from the time at 1 ns to 10 ns. All the spectra in figure 9(b) thus includes multiple frequency components because the receiver at each location can receive all the frequencies from all the emitter locations. Location A is close to the anode. Therefore, the high frequency components have high power densities. The spectrum does not change significantly when the time runs to 10 ns. This agrees with the electron density evolution shown in figure 7(c) that the high electron density region always exits next to the anode, while the evolutions of other low electron density regions are further from Location A and thus have less contribution to the spectra. Interestingly, multiple peaks can be found in the spectra. Location B is shown in the second column, and it is close to the middle part of the plasma jet. Therefore, the spectra of Location B have the highest peak in the middle, around 16 GHz. However, at the end of the frequency axis, around 30 GHz, there is another increasing trend. This is not surprising because the high frequency is due to the high electron density that is supposed to provide high power. However, this relation is not significant in Location A's column because Location A is closer to the high electron density region. On the other hand, while the time runs to 10 ns, the total power of Location B rises. This agrees with the streamer propagation in that the propagation passes through the plasma jet axis and raises the electron density. More electrons oscillating means higher power. Location C is close to the plasma jet tip where fewer electrons exist, leading to a low frequency peak at around 5 GHz. The high electron density region contributes less but leads to another high-power peak at the high frequencies. Overall, Location C's spectra and the total power density at this location are much lower. The temporal evolution of Location C's spectrum is also interesting. When the streamer is propagating towards the plasma jet tip, the electron density at the tip increases. This does not only mean that the low-frequency peak in the spectra of Location C is raised but also shifts to the high-frequency direction. This is also because of the relation between the plasma oscillation frequency and the electron density as shown in equation (22). As a result, when time goes by, the low-frequency peak disappears but the total power increases.

The experimental result can thus be used to verify a part of the above ideas. As shown in figure 10, the plasma oscillation power spectrum is measured from 12 GHz to 16 GHz. The signal is relatively flat within about 12–13 GHz and starts to raise at about 14 GHz, from 2 W cm<sup>-2</sup> to 3 W cm<sup>-2</sup>. However, because the WR 75 horn antenna is several centimeters wide, we do not have spatial resolution. This result is thus compared with the spatially integrated results of the simulation over the location from A to C, which is also shown in figure 10. The simulation result also shows a flat pattern within 12–14 GHz at about 2 W cm<sup>-2</sup> and then raise to about 3 W cm<sup>-2</sup>. Therefore, the experimental results agree well with the simulation.

The spectrum of the plasma oscillation as the conditions of different discharge voltages is also tested in the simulation as displayed in figure 11. Increasing the discharge voltage of the plasma jet causes more electric energy to convert to the radiation energy. As the discharge voltage is larger, the electron density and electron velocity of the plasma jet is greater, and thus the power density of the radiation field is larger in this



**Figure 9.** The spatially and temporally resolved plasma oscillation power spectra. (a) The three locations of analysis are shown in a background of total power density distribution at 4 ns. (b) The temporally resolved spectra.



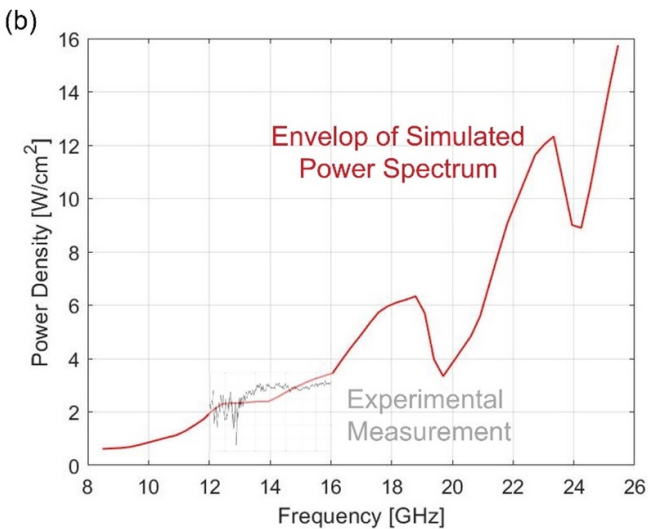


**Figure 10.** The power density comparison between the (a) experimental observation and (b) the simulation results which is the envelop of the simulated data as a spatial integral over the location A to C.

case. In addition, increasing the discharge voltage also makes the peaks of the spectrum shift right. As the discharge voltage increases from 6000 V to 8000 V, the maximum power density in each spectrum approximately increases about 1.8 times, and the maximum frequency is increased by 0.91 GHz.

Finally, figure 12 displays the curves of power density produced by the plasma jet bremsstrahlung emission at a time of 4 ns, and only the values of the cells with the top 70% electron density are shown here. The curve color corresponds to the color of the electron density image in the subplot, which indicates the cell locations where the curves are generated. For example, the yellow curve is produced by the yellow cell which has a greater electron density near the high-voltage electrode. In general, the plasma jet cell with a greater electron density produces a larger power density. Also, figure 12 displays that the power density is proportional

to the frequency, and the power density value is on the order of  $10^{-7}$  W cm<sup>-2</sup> within 100 GHz frequency. This power density is too low compared with the one produced by plasma oscillations. Therefore, the bremsstrahlung emission is also neglectable in the total microwave radiation of the plasma jet.

#### 4.3. The physical dose of plasma medicine

The simulations presented in this paper indicates that the plasma oscillation power density is playing the major role in the GHz emissions, while the bulk current and the bremsstrahlung emissions have neglectable power. Meanwhile, in other studies, it has been shown that the discharge frequency of plasma has significant physical effects in plasma biomedical applications, such as the sensitization and cell membrane damage [17, 41], not only for the cancerous cells, but also for the blood cells and skin tissues according to some recent studies [42, 43]. However, the exact physical effects of the GHz emissions are still unknown. Although the detailed physical mechanism of the GHz emissions treatments is not yet fully discovered, the dose of such a physical emission can be quantified based on the power spectrum of the EM emission. The physical dose is a cocktail of multiple frequencies and we expect each of frequency may have unique physical effect. This is also similar to the well-known chemical products of CAP which is a cocktail of multiple different RONS with each has different chemical and inner cellular pathways.

According to the theory of electrical impedance spectroscopy of cells, the GHz emission, corresponding to the gamma dispersion, may have relation to the molecular level objects, while we have shown that the discharge frequency corresponding to the beta dispersion at kHz—MHz can resonant the transmembrane potential polarization [44-46]. While the gamma dispersion is not directly indicative of the size of a particular structure in the sample, changes in the dispersion's characteristics are related to the alterations in the diffusion properties of ions and molecules transports. This implies that the GHz physical dose can (1) alter the extracellular matrix components presenting at the vicinity of cells, such as the ion cloud near cells in the medium; (2) directly modulate the ion transportation in and out of the cell membrane, not due to the interactions with the membranes but with the ions. These effects will further alter the inner cellular metabolism through its energy production pathways (e.g. glycolysis, oxidative phosphorylation).

However, the plasma jets are usually not free jets but impinging jets during the working period in biomedical applications and material processing [47, 48]. The impinging gas flow and the impact of streamer on an interface may or may not alter the RF emission spectrum. If the target surface is conductive or at a lower potential, there will be a reflection of the streamer namely 'return stroke' which may also alter the emission [49, 50]. Therefore, this work is giving a general concept of methods to quantify the emission of a plasma jet with an of the free jet. Investigations on specific plasma jet

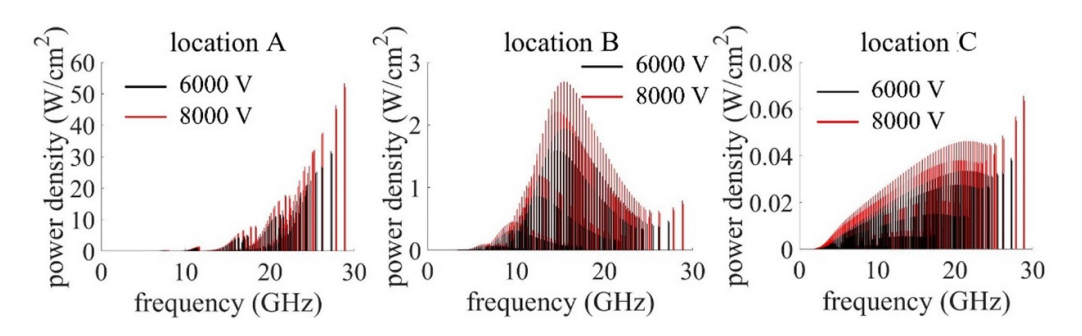


Figure 11. Power density spectra when varying the discharge voltage.

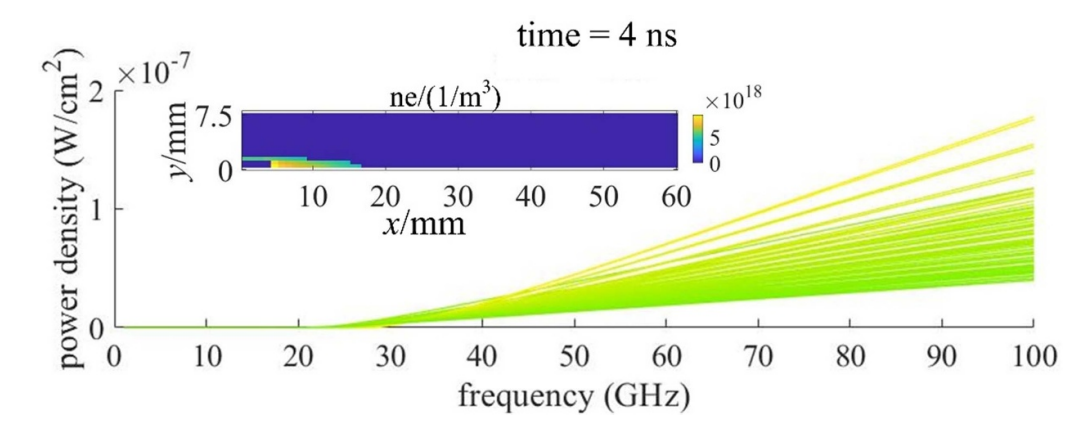


Figure 12. Power density spectra of the plasma jet bremsstrahlung emission.

scenarios can be done using the same method. We will study the emission from the impinging spot in the future.

#### 5. Conclusion

In this work, we quantify the power density spectra of the plasma jet with temporal resolution and spatial resolution for both the emission locations and the receiver locations. Since these resolutions are not available in the experiments, simulation is a very valuable tool to support the physical effects of plasma medical applications.

After modeling the 2D streamer propagation of a heliumair plasma jet, we considered three types of emissions in 3D computations. Both the bulk current emissions and the bremsstrahlung emissions have significantly lower power compared with the plasma oscillation emissions. Therefore, our first conclusion is that plasma oscillation is playing a major role in the physical effects of plasma medical applications. By analyzing the spectra at multiple receiver locations, we also conclude that the distribution of electron density along the plasma jet can provide a continuous spectrum. However, different receiver locations may receive different spectra, depending on the distance to the anode and the plasma jet tip. The spectra can also change during the streamer propagation and increasing the electron density can not only increase the power density but also shift the low frequency peaks. Finally, the power density value can go up to 60 W cm<sup>-2</sup> near the anode for 30 GHz and a high discharge voltage at 8000 V, but on average, the value in simulation is close to what we measured experimentally at around 2 W  $\rm cm^{-2}$  to 3 W  $\rm cm^{-2}$ .

Overall, as more discussions of the physical effects in the plasma medicine community are taken place, the quantification of CAP RF emissions becomes urgent. This work is thus timely filling the gap of what is emitting from the CAP during a direct treatment. This will help the plasma researchers to understand: (1) the physical radiation dose of the plasma medical therapy, (2) the basis to find the optimization of the therapy, and the control of the CAP generator. In the future, the reactive species will be considered along with the RF power density spectra for understanding plasma medical applications, not only for the cancer therapy, but may be informative for wound treatments, sterilizations, etc. Also, we will investigate the MHz and kHz emissions in the future works, as well as different CAP setups such as the impinging jet, using a nanosecond power supply, and different gases. The RF emissions in the dark period after the streamer propagation is also an interesting topic. However, at the current stage, we focus on the relation between the RF emissions and the streamer propagation. We would like to leave the study of the dark period emissions in a future work.

#### Data availability statement

The data that support the findings of this study are openly available at the following URL/DOI: https://mpnl.seas.gwu.edu/open-codes/.

#### Acknowledgments

This work is supported by the China Scholarship Council (No. 201906840027) and the National Science Foundation of USA (Grants 1747760 and 1919019).

#### **ORCID iDs**

Yi Liu https://orcid.org/0000-0002-6941-0679 Li Lin https://orcid.org/0000-0003-0176-8858 Michael Keidar https://orcid.org/0000-0003-0869-4310

#### References

- [1] Bekeschus S, Favia P, Robert E and Von Woedtke T 2019 White paper on plasma for medicine and hygiene: future in plasma health sciences *Plasma Process. Polym.* **16** 1800033
- [2] Lu X et al 2022 Grand challenges in low temperature plasmas Front. Phys. 10 1040658
- [3] Dobrynin D, Fridman G, Friedman G and Fridman A 2009 Physical and biological mechanisms of direct plasma interaction with living tissue New J. Phys. 11 115020
- [4] Pereira S, Pinto E, Ribeiro P A and Sério S 2019 Study of a cold atmospheric pressure plasma jet device for indirect treatment of squamous cell carcinoma Clin. Plasma Med. 13 9–14
- [5] Thiyagarajan M, Sarani A and Gonzalez X 2012 Characterization of portable resistive barrier plasma jet and its direct and indirect treatment for antibiotic resistant bacteria and THP-1 leukemia cancer cells *IEEE Trans*. *Plasma Sci.* 40 3533–45
- [6] Malyavko A, Yan D, Wang Q, Klein A L, Patel K C, Sherman J H and Keidar M 2020 Cold atmospheric plasma cancer treatment, direct versus indirect approaches *Mater*. Adv. 1 1494–505
- [7] Saadati F, Mahdikia H, Abbaszadeh H-A, Abdollahifar M-A, Khoramgah M S and Shokri B 2018 Comparison of direct and indirect cold atmospheric-pressure plasma methods in the B16F10 melanoma cancer cells treatment *Sci. Rep.* 8 7689
- [8] Yan D, Wang Q, Adhikari M, Malyavko A, Lin L, Zolotukhin D B, Yao X, Kirschner M, Sherman J H and Keidar M 2020 A physically triggered cell death via transbarrier cold atmospheric plasma cancer treatment ACS Appl. Mater. Interfaces 12 34548–63
- [9] Adamovich I et al 2022 The 2022 plasma roadmap: low temperature plasma science and technology J. Phys. D: Appl. Phys. 55 373001
- [10] Laroussi M et al 2022 Low-temperature plasma for biology, hygiene, and medicine: perspective and roadmap IEEE Trans. Radiat. Plasma Med. Sci. 6 127–57
- [11] Yan D, Wang Q, Malyavko A, Zolotukhin D B, Adhikari M, Sherman J H and Keidar M 2020 The anti-glioblastoma effect of cold atmospheric plasma treatment: physical pathway v.s. chemical pathway Sci. Rep. 10 11788
- [12] Lu X, Naidis G V, Laroussi M and Ostrikov K 2014 Guided ionization waves: theory and experiments *Phys. Rep.* 540 123–66
- [13] Lin L, Lyu Y, Trink B, Canady J and Keidar M 2019 Cold atmospheric helium plasma jet in humid air environment J. Appl. Phys. 125 153301
- [14] Breden D, Miki K and Raja L L 2011 Computational study of cold atmospheric nanosecond pulsed helium plasma jet in air Appl. Phys. Lett. 99 111501

- [15] Norberg S A, Johnsen E and Kushner M J 2015 Helium atmospheric pressure plasma jets touching dielectric and metal surfaces J. Appl. Phys. 118 013301
- [16] Shashurin A, Shneider M N and Keidar M 2012 Measurements of streamer head potential and conductivity of streamer column in cold nonequilibrium atmospheric plasmas *Plasma Sources Sci. Technol.* 21 034006
- [17] Lin L et al 2023 Cell membrane oscillations under radiofrequency electromagnetic modulation Langmuir 39 3320–31
- [18] Cheng H, Xu J, Li X, Liu D and Lu X 2020 On the dose of plasma medicine: equivalent total oxidation potential (ETOP) Phys. Plasmas 27 063514
- [19] Gidon D, Graves D B and Mesbah A 2019 Predictive control of 2D spatial thermal dose delivery in atmospheric pressure plasma jets *Plasma Sources Sci. Technol.* 28 085001
- [20] Wu S, Huang Q, Wang Z and Lu X 2013 On the magnetic field signal radiated by an atmospheric pressure room temperature plasma jet J. Appl. Phys. 113 043305
- [21] Lin L, Lyu Y, Shneider M N and Keidar M 2018 Average electron temperature estimation of streamer discharge in ambient air Rev. Sci. Instrum. 89 113502
- [22] Schröter S, Gibson A R, Kushner M J, Gans T and O'Connell D 2018 Numerical study of the influence of surface reaction probabilities on reactive species in an rf atmospheric pressure plasma containing humidity *Plasma Phys. Control. Fusion* 60 014035
- [23] Sakiyama Y, Graves D B, Chang H-W, Shimizu T and Morfill G E 2012 Plasma chemistry model of surface microdischarge in humid air and dynamics of reactive neutral species J. Phys. D: Appl. Phys. 45 425201
- [24] Norberg S A, Johnsen E and Kushner M J 2015 Formation of reactive oxygen and nitrogen species by repetitive negatively pulsed helium atmospheric pressure plasma jets propagating into humid air *Plasma Sources Sci. Technol*. 24 035026
- [25] Hagelaar G J M and Pitchford L C 2005 Solving the Boltzmann equation to obtain electron transport coefficients and rate coefficients for fluid models *Plasma Sources Sci. Technol.* 14 722–33
- [26] Carbone E, Graef W, Hagelaar G, Boer D, Hopkins M M, Stephens J C, Yee B T, Pancheshnyi S, van Dijk J and Pitchford L 2021 Data needs for modeling low-temperature non-equilibrium plasmas: the LXCat project, history, perspectives and a tutorial Atoms 9 16
- [27] Balanis C A 2015 Antenna Theory Analysis and Design (Wiley)
- [28] Lamoureux M 2000 Interest of electron—ion bremsstrahlung for plasma physics *Radiat. Phys. Chem.* 59 171–80
- [29] He W, Liu X, Xian R, Chen S, Liao R, Yang F and Xiao H 2013 Kinetics characteristics and bremsstrahlung of argon dc discharge under atmospheric pressure *Plasma Sci. Technol.* 15 335–42
- [30] Lin L, Yan D, Gjika E, Sherman J H and Keidar M 2019 Atmospheric plasma meets cell: plasma tailoring by living cells ACS Appl. Mater. Interfaces 11 30621–30
- [31] Bohm D and Gross E P 1949 Theory of plasma oscillations. B. Excitation and damping of oscillations *Phys. Rev.* 75 1864–76
- [32] Befki G 1966 Radiation Processes in Plasmas (Wiley)
- [33] Naidis G V 2012 Modeling of helium plasma jets emerged into ambient air: influence of applied voltage, jet radius, and helium flow velocity on plasma jet characteristics *J. Appl. Phys.* 112 103304
- [34] Lin P, Zhang J, Nguyen T, Donnelly V M and Economou D J 2021 Numerical simulation of an atmospheric pressure plasma jet with coaxial shielding gas J. Phys. D: Appl. Phys. 54 075205

- [35] Naidis G V 2010 Modelling of streamer propagation in atmospheric-pressure helium plasma jets J. Phys. D: Appl. Phys. 43 402001
- [36] Brok W J M, Bowden M D, Van Dijk J, Van Der Mullen J J A M and Kroesen G M W 2005 Numerical description of discharge characteristics of the plasma needle J. Appl. Phys. 98 013302
- [37] Liu X Y, Pei X K, Lu X P and Liu D W 2014 Numerical and experimental study on a pulsed-dc plasma jet *Plasma* Sources Sci. Technol. 23 035007
- [38] Van Der Schans M, Platier B, Koelman P, van de Wetering F, van Dijk J, Beckers J, Nijdam S and IJzerman W 2019 Decay of the electron density and the electron collision frequency between successive discharges of a pulsed plasma jet in N<sub>2</sub> Plasma Sources Sci. Technol. 28 035020
- [39] Shashurin A, Shneider M N, Dogariu A, Miles R B and Keidar M 2009 Temporal behavior of cold atmospheric plasma jet Appl. Phys. Lett. 94 231504
- [40] Lin L and Keidar M 2016 Cold atmospheric plasma jet in an axial DC electric field *Phys. Plasmas* 23 083529
- [41] Yao X, Lin L, Soni V, Gjika E, Sherman J H, Yan D and Keidar M 2020 Sensitization of glioblastoma cells to temozolomide by a helium gas discharge tube *Phys. Plasmas* 27 114502
- [42] Vijayarangan V, Delalande A, Dozias S, Pouvesle J-M, Pichon C and Robert E 2018 Cold atmospheric plasma parameters investigation for efficient drug delivery in HeLa cells IEEE Trans. Radiat. Plasma Med. Sci. 2 109–15
- [43] Vijayarangan V, Dozias S, Heusèle C, Jeanneton O, Nizard C, Pichon C, Pouvesle J M, Stancampiano A and Robert E

- 2023 Boost of cosmetic active ingredient penetration triggered and controlled by the delivery of kHz plasma jet on human skin explants *Front. Phys.* **11** 1173349
- [44] Qiao G, Duan W, Chatwin C, Sinclair A and Wang W 2010 Electrical properties of breast cancer cells from impedance measurement of cell suspensions J. Phys.: Conf. Ser. 224 012081
- [45] Lin L, Hou Z, Yao X, Liu Y, Sirigiri J R, Lee T and Keidar M 2020 Introducing adaptive cold atmospheric plasma: the perspective of adaptive cold plasma cancer treatments based on real-time electrochemical impedance spectroscopy *Phys. Plasmas* 27 063501
- [46] Rojas J E P Design of a wide tuning-range CMOS 130-nm quadrature VCO for cell impedance spectroscopy *6th IEEE Germany Student Conf. Proc.* pp 7–12
- [47] Klarenaar B L M, Guaitella O, Engeln R and Sobota A 2018 How dielectric, metallic and liquid targets influence the evolution of electron properties in a pulsed He jet measured by Thomson and Raman scattering *Plasma Sources Sci. Technol.* 27 085004
- [48] Darny T, Pouvesle J-M, Puech V, Douat C, Dozias S and Robert E 2017 Analysis of conductive target influence in plasma jet experiments through helium metastable and electric field measurements *Plasma Sources Sci. Technol.* 26 045008
- [49] Robert E, Darny T, Dozias S, Iseni S and Pouvesle J M 2015 New insights on the propagation of pulsed atmospheric plasma streams: from single jet to multi jet arrays *Phys. Plasmas* 22 122007
- [50] Sigmond R S 1984 The residual streamer channel: return strokes and secondary streamers *J. Appl. Phys.* **56** 1355–70